



Improvement of the magnetoelectric response in $\text{NiFe}_2\text{O}_4\text{--Sr}_{0.5}\text{Ba}_{0.5}\text{Nb}_2\text{O}_6$ composites using LiNbO_3 as sintering additive

Roberto Köferstein^{*}, Stefan G. Ebbinghaus

Institute of Chemistry, Martin Luther University Halle-Wittenberg, Kurt-Mothes-Straße 2, 06120 Halle, Germany

ARTICLE INFO

Keywords:

Magnetoelectric effect
Niobite
Multiferroic materials
Ferrite
Sintering additive

ABSTRACT

Magnetoelectric $(\text{NiFe}_2\text{O}_4)_{0.3}\text{--}(\text{Sr}_{0.5}\text{Ba}_{0.5}\text{Nb}_2\text{O}_6)_{0.7}$ composites with addition of LiNbO_3 as sintering additive were prepared by a classical mixed-oxide method. XRD patterns of ceramics sintered between 1000 and 1200 °C show the desired $\text{Sr}_{0.5}\text{Ba}_{0.5}\text{Nb}_2\text{O}_6$ and NiFe_2O_4 phases. SEM investigations confirm the 0–3 connectivity of the composite ceramics. The addition of 10 and 20 mol% LiNbO_3 improves the densification of the composite ceramics and leads to an increase of the size of the $\text{Sr}_{0.5}\text{Ba}_{0.5}\text{Nb}_2\text{O}_6$ grains. Magnetic measurements show hystereses with low coercivities. Dielectric measurements were carried out depending on temperature and frequency. The samples with the LiNbO_3 addition show significantly higher resistivity values (σ_{DC}). Magnetoelectric measurements were carried out in dependence of the magnetic DC-field, temperature, and frequency. The maximum magnetoelectric coefficient (α_{ME}) rises with the addition of LiNbO_3 from 180 to 803 $\mu\text{V Oe}^{-1} \text{cm}^{-1}$ (@900 Hz). Temperature dependent measurements show a continuously decreasing of α_{ME} with lower temperature.

1. Introduction

Materials, which exhibits at least two ferroic orderings are called multiferroics. The interaction between such ferroic phenomena (e.g. ferromagnetism, ferroelectricity, ferroelasticity) leads to new functionalities and applications. The magnetoelectric effect (ME) as a result of coupling between ferro-/ferrimagnetism and ferroelectricity was first investigated by Astrov [1] and allows to control the electrical polarization by a magnetic field (direct ME effect) or the magnetization by an electric field (indirect ME effect). Composite materials composed of a ferrimagnetic and a ferroelectric phase often show strong magnetoelectric effects at room temperature in contrast to single-phase ME materials like BiFeO_3 or Cr_2O_3 [2,3]. The coupling between the two phases is mediated by their interfaces. The two different phases in such composites can be arranged in various connectivities, denoted as 0–3, 2–2, 1–3, and 3–3, in which the numbers reflect the dimension in which each phase is self-connected [4]. 0–3 composites show magnetoelectric coefficients of few $\mu\text{V Oe}^{-1} \text{cm}^{-1}$ at low H_{AC} frequencies up to several $\text{V Oe}^{-1} \text{cm}^{-1}$ at resonance conditions ($> 10 \text{ kHz}$) [5–8]. Composites on the basis of PbTiO_3 show large magnetoelectric coefficients [9–11]. Due to the harmful environmental effect of lead containing compounds, composites with e.g. BaTiO_3 as lead-free piezoelectric compound have been extensively investigated [12–16]. In contrast, magnetoelectric

composites with $\text{Sr}_{0.5}\text{Ba}_{0.5}\text{Nb}_2\text{O}_6$ (SBN) as ferroelectric phase are less well studied [17–19]. $\text{Sr}_{0.5}\text{Ba}_{0.5}\text{Nb}_2\text{O}_6$ crystallizes in the open tungsten-bronze structure and shows a ferroelectric relaxor behavior with a diffuse phase transition around 120 °C [20–22]. In contrast to composites with BaTiO_3 , the ferroelectric phase of $\text{Sr}_{0.5}\text{Ba}_{0.5}\text{Nb}_2\text{O}_6$ is stable even after sintering at high temperatures [23–27]. Sintering of magnetoelectric composites often results in an insufficient densification at lower temperatures. On the other hand, higher firing temperatures often lead to an increase of the conductivity, resulting in lower magnetoelectric coefficients [28]. Some authors used sintering additives to improve the densification of magnetoelectric composites [9, 29–33]. However, to our best knowledge, systematic investigations of the influence of sintering additives on the magnetoelectric behavior have not been reported so far.

The aim of this work is to examine the influence of LiNbO_3 on the magnetoelectric properties of $(\text{NiFe}_2\text{O}_4)_{0.3}\text{--}(\text{Sr}_{0.5}\text{Ba}_{0.5}\text{Nb}_2\text{O}_6)_{0.7}$ composites. The magnetoelectric samples were synthesized by the conventional mixed-oxide method. Phase evolution and microstructure of the ceramics were monitored by XRD and SEM. The magnetoelectric behavior was investigated depending on H_{DC} , frequency of H_{AC} and temperature. Additionally the composite were characterized by impedance spectroscopy and magnetic measurements.

^{*} Corresponding author.

E-mail address: roberto.koefenstein@chemie.uni-halle.de (R. Köferstein).

<https://doi.org/10.1016/j.jeurceramsoc.2023.06.040>

Received 8 February 2023; Received in revised form 22 May 2023; Accepted 14 June 2023

Available online 15 June 2023

0955-2219/© 2023 The Author(s). Published by Elsevier Ltd. This is an open access article under the CC BY license (<http://creativecommons.org/licenses/by/4.0/>).

2. Experimental

2.1. Material preparation

We prepared $(\text{NiFe}_2\text{O}_4)_{0.3}\text{--}(\text{Sr}_{0.5}\text{Ba}_{0.5}\text{Nb}_2\text{O}_6)_{0.7}$ composites (= 20.30 wt% NiFe_2O_4), abbreviated as NF-SBN. For the composites with the sintering additive (LiNbO_3) we added 10 and 20 mol% LiNbO_3 , related to the amount of $\text{Sr}_{0.5}\text{Ba}_{0.5}\text{Nb}_2\text{O}_6$, resulting in a nominal composition of $(\text{NiFe}_2\text{O}_4)_{0.3}\text{--}(\text{Sr}_{0.5}\text{Ba}_{0.5}\text{Nb}_2\text{O}_6 + x \text{LiNbO}_3)_{0.7}$ ($x = 0.1$; 0.2), abbreviated as NF-SBN+LN-0.1 and NF-SBN+LN-0.2 (= 19.73 wt% and 19.16 wt% NiFe_2O_4).

Fig. S1 (supporting information) shows the preparation scheme of the composite powders. The samples were synthesized by the conventional mixed-oxide method. The oxides and carbonates were mixed and milled in a planetary mill for 4 h using polyamide jars, ZrO_2 -balls, and propan-2-ol. To prepare NiFe_2O_4 (NF), NiO (Berlin-Chemie, puriss.) and Fe_2O_3 (Alfa Aesar, 99.9 %) were mixed in a molar ratio of 1:1. After filtering and drying the mixture was calcined in static air at 1150 °C for 2 h (heating rate 10 K min^{-1}). $\text{Sr}_{0.5}\text{Ba}_{0.5}\text{Nb}_2\text{O}_6$ (SBN) was synthesized by milling stoichiometric amounts of BaCO_3 (Merck, > 98.5 %), SrCO_3 (Sigmar-Aldrich, 99.9 %), and Nb_2O_5 (Alpha Aesar, 99.9 %) and calcining at 1200 °C for 5 h (heating rate 10 K min^{-1}). According to the desired composition NiFe_2O_4 and $\text{Sr}_{0.5}\text{Ba}_{0.5}\text{Nb}_2\text{O}_6$ (30 mol% NiFe_2O_4) were mixed in a polyamide jar (ZrO_2 -balls, propan-2-ol) to obtain NF-SBN composite powders.

Composites with the sintering additive LiNbO_3 (NF-SBN+LN- x) were synthesized as follows. BaCO_3 , SrCO_3 , Nb_2O_5 and Li_2CO_3 (UCB SA, ≥ 99 %) were mixed together and calcined at 1200 °C for 3 h. Here, the fractions of Ba, Sr, Nb, and Li were calculated as $n_{\text{Ba}} = n_{\text{Sr}} = n_{\text{Nb}}/(2[2 + x])$ and $n_{\text{Li}} = n_{\text{Nb}} x/(2 + x)$ ($x = 0.1$ and 0.2; molar addition of LiNbO_3 related to the amount of $\text{Sr}_{0.5}\text{Ba}_{0.5}\text{Nb}_2\text{O}_6$) resulting in a nominal composition of $\text{Sr}_{0.5}\text{Ba}_{0.5}\text{Nb}_2\text{O}_6 + x \text{LiNbO}_3$ (SBN+LN- x). To obtain NF-SBN+LN- x composites, NiFe_2O_4 and $\text{Sr}_{0.5}\text{Ba}_{0.5}\text{Nb}_2\text{O}_6 + x \text{LiNbO}_3$ powders (30 mol% NiFe_2O_4 related to $\text{Sr}_{0.5}\text{Ba}_{0.5}\text{Nb}_2\text{O}_6$) were mixed together as described above. All composite powders were mixed with 10 wt% of a saturated aqueous polyvinyl alcohol (PVA) solution as a pressing aid and uniaxially pressed at about 140 MPa into pellets (green density: 3.1 g cm^{-3}). These pellets were sintered to ceramic bodies on a ZrO_2 fibre mat between 1000 and 1200 °C (heating-/cooling rate 5 K min^{-1}) with a soaking time of 1 h.

2.2. Characterization

X-ray powder diffraction patterns were recorded at room temperature on a Bruker D8-Advance diffractometer, equipped with a one-dimensional silicon strip detector (LynxEye™) using $\text{Cu-K}\alpha$ radiation and a counting time of 1 s per data point. Scanning electron microscope images were collected with a Phenom ProX SEM in the backscattered electron mode (BSE). Magnetic and magnetoelectric measurements were carried out using a Quantum Design PPMS9. Magnetic hysteresis loops were taken at 300 K with magnetic DC field cycling between –90 and +90 kOe. The samples were enclosed in gel capsules whose very small diamagnetic contribution was subtracted during data evaluation. For magnetoelectric and impedance measurements, ceramic bodies were sputtered on both sides with 100 nm thick gold electrodes using a Cressington Sputter Coater 108auto. For magnetoelectric measurements the samples were electrically poled for 18 h at room temperature applying an electric field of about 6 kV cm^{-1} with a current limit of 0.1 mA. Afterwards, the poled samples were short-circuited for 5 min. The magnetoelectric measurements were performed using a self-made setup [15] with the magnetic DC field parallel to the electrical polarization and a small AC driving field of about 8 Oe was superimposed collinearly to the static field by a solenoid. The in-phase voltage (U_{ME}) was recorded using the lock-in technique. The magnetoelectric coefficient (α_{ME}) was calculated as $\alpha_{\text{ME}} = U_{\text{ME}} \cdot (\text{H}_{\text{AC}} \cdot d)^{-1}$ with d being the sample thickness. The thickness of the ceramic samples is between 0.93 and 1.02 mm. The

magnetoelectric behavior was investigated at 300 K using a DC field cycling between ± 15 kOe and $\nu(\text{H}_{\text{AC}}) = 900$ Hz. Frequency- and temperature-dependent measurements were done at the DC field at which the maximum of α_{ME} was found. An Impedance Analyzer 4192 A (Hewlett Packard) was used for frequency- and temperature-dependent impedance measurements.

3. Results and discussion

3.1. Synthesis, sintering, microstructure, and phase composition of the ceramics

$(\text{NiFe}_2\text{O}_4)_{0.3}\text{--}(\text{Sr}_{0.5}\text{Ba}_{0.5}\text{Nb}_2\text{O}_6)_{0.7}$ composites (NF-SBN) and composites with addition of 10 and 20 mol% LiNbO_3 , related to $\text{Sr}_{0.5}\text{Ba}_{0.5}\text{Nb}_2\text{O}_6$, $(\text{NiFe}_2\text{O}_4)_{0.3}\text{--}(\text{Sr}_{0.5}\text{Ba}_{0.5}\text{Nb}_2\text{O}_6 + x \text{LiNbO}_3)_{0.7}$ (NF-SBN+LN- x , $x = 0.1$; 0.2), were prepared by the conventional mixed-oxide method. The composite powders were pressed to pellets and sintered in static air between 1000 and 1200 °C for 1 h (heating-/cooling rate: 5 K min^{-1}). Fig. 1 exemplarily shows the XRD patterns after sintering of compacted composite powders at 1050 and 1200 °C. All composite ceramics show the reflections of cubic NiFe_2O_4 (JCPDS #01-074-2081) and tetragonal $\text{Sr}_{0.5}\text{Ba}_{0.5}\text{Nb}_2\text{O}_6$ (JCPDS #01-074-6520). The XRD patterns of NF-SBN+LN-0.1 and NF-SBN+LN-0.2 do not show any peaks of LiNbO_3 . As pointed out in our previous paper [34], firing of $\text{Sr}_{0.5}\text{Ba}_{0.5}\text{Nb}_2\text{O}_6$ and LiNbO_3 results in the formation of the solid solution $(\text{Li}_y(\text{Sr}_{0.5}\text{Ba}_{0.5})_{1-y/2}\text{Nb}_2\text{O}_6)$, $y = x/(1 + x/2)$ with a tetragonal tungsten-bronze structure. Additionally, the XRD investigations reveal the formation of secondary phases. Upon sintering below 1100 °C two weak reflections at 24.7° and 30.5° point the formation of monoclinic FeNbO_4 (wolframite structure, JCPDS #01-071-1849) or orthorhombic FeNb_2O_6 or NiNb_2O_6 (JCPDS #01-075-2158 and #01-076-2354) with columbite structure. These reflections disappear completely after sintering at 1150 °C and 1200 °C. On the other hand, new peaks at 35.0°, 55.1°, and a raised intensity at 26.7° indicate either the formation of tetragonal FeNbO_4 [JCPDS #00-016-0357] or tetragonal FeNb_2O_6 or NiNb_2O_6 [JCPDS #01-077-1290 and #01-076-2355] with a metal-disordered rutile structure. The fraction of the secondary phase in the samples amounts to 2–4 wt% for sintering between 1050 and 1200 °C, whereas after firing at 1000 °C that fraction is considerably less than 2 wt%. EDX investigations (see below) on several grains show that

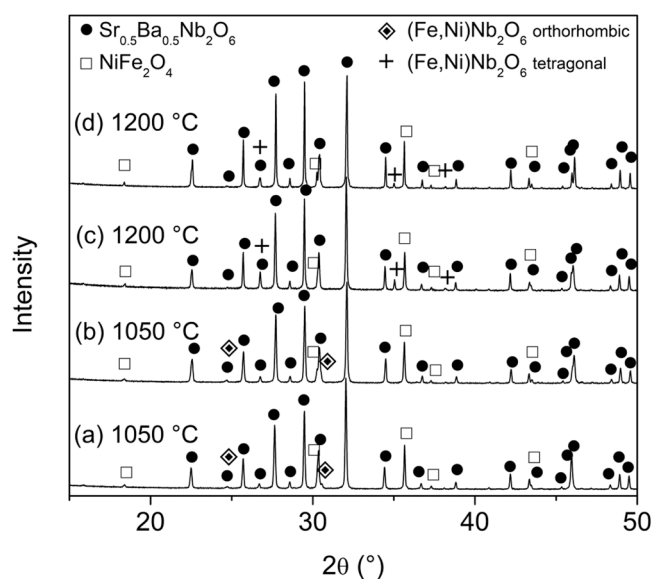


Fig. 1. Room-temperature XRD patterns of SBN+LN- x composite ceramics after sintering at the indicated temperatures for 1 h (heating-/cooling rate 5 K min^{-1}). (a,c) NF-SBN, (b,d) NF-SBN+LN-0.2.

the secondary phases consist of Ni, Fe and Nb in an atomic ratio of about Fe/Ni \approx 1.3–1.5 and Nb/(Fe+Ni) \approx 2. Therefore, the composition of the secondary phases can be approximately described as $\text{Fe}_{0.6}\text{Ni}_{0.4}\text{Nb}_2\text{O}_6$ which corresponds, according to the XRD results, to the columbite structure for sintering temperatures below 1100 °C which transforms into the rutile structure at higher temperatures.

The bulk densities of the dark-grey or black sintered bodies were calculated from their weight and geometric dimension. The relative bulk densities were related to 5.37 g cm^{-3} , because the single crystal densities of $\text{Sr}_{0.5}\text{Ba}_{0.5}\text{Nb}_2\text{O}_6$ and NiFe_2O_4 are 5.37 g cm^{-3} and 5.38 g cm^{-3} , respectively [22,35]. As seen in Fig. 2 the composite ceramic bodies with sintering additive (NF-SBN+LN- x) show considerably higher densities compared to pure NF-SBN ceramics. In contrast to NF-SBN and NF-SBN+LN-0.1, the density of NF-SBN+LN-0.2 ceramics does not significantly change upon rising the sintering temperature from 1150° to 1200°C due to the appearance of larger pillar-like grains compared to the NF-SBN and NF-SBN+LN-0.1 ceramics as described below. After sintering at 1200 °C, all samples show relative densities of $\geq 90 \%$.

Typical microstructures of the composite ceramics are shown in Fig. 3. The SEM images were recorded in the BSE mode, therefore the bright grains are $\text{Sr}_{0.5}\text{Ba}_{0.5}\text{Nb}_2\text{O}_6$ (SBN) and the dark ones corresponds to NiFe_2O_4 (NF) and secondary phases, respectively. Representative EDX spectra are shown in Figs. S2 and S3 (supporting information) and confirm the presence of $\text{Sr}_{0.5}\text{Ba}_{0.5}\text{Nb}_2\text{O}_6$ and NiFe_2O_4 . Measurements on several large grains point to an iron doping ($< 1 \text{ at}\%$) of the $\text{Sr}_{0.5}\text{Ba}_{0.5}\text{Nb}_2\text{O}_6$ phase. According to Reverz et al. [36] and Neurgaonkar et al. [37], Fe^{3+} prefers to occupy the Nb^{5+} sites. On the other hand, traces of Sr and Nb in the NiFe_2O_4 spectrum are most likely caused by the relative large interaction volume of the electron beam compared to the small grain size. The EDX spectra of the secondary phase reveal the composition of $\text{Fe}_{0.6}\text{Ni}_{0.4}\text{Nb}_2\text{O}_6$, as discussed above.

The shape of the NiFe_2O_4 grains is mainly irregular after sintering at 1000 °C and changes to a pyramidal-/octahedral-like one for higher temperatures. Grains of the secondary phase show an irregular shape in all ceramics with sizes up to about 10 μm . Up to a sintering temperature of 1100 °C, $\text{Sr}_{0.5}\text{Ba}_{0.5}\text{Nb}_2\text{O}_6$ forms globular and irregular grains. Starting at 1150 °C, $\text{Sr}_{0.5}\text{Ba}_{0.5}\text{Nb}_2\text{O}_6$ additionally forms pillar-shaped grains besides the globular-/irregular grains. The fraction of these pillars increases significantly after sintering at 1200 °C. We observe a considerable increase of the SBN grain size both with sintering temperature (T_s) and LiNbO_3 addition (x). For $T_s = 1000 \text{ °C}$, the globular-/irregular SBN grains are between 0.6 and 5 μm (NF-SBN), 0.7–7 μm (NF-SBN+LN-0.1), and 1–13 μm (NF-SBN+LN-0.2) which increase to 1–6 μm (NF-SBN), 1.1–10 μm (NF-SBN+LN-0.1), and 1.4–16 μm (NF-SBN+LN-0.2) for $T_s = 1100 \text{ °C}$. After firing at 1200 °C, the ceramics consist of globular grains of sizes between 1.2 and 11 μm , 1.5–12 μm ,

and 4–30 μm , whereas the pillar-like grains have dimensions of about $4\text{--}15 \times 2\text{--}4 \mu\text{m}$, $5\text{--}11 \times 3\text{--}4 \mu\text{m}$, and $6\text{--}25 \times 4\text{--}12 \mu\text{m}$ for NF-SBN, NF-SBN+LN-0.1, and NF-SBN+LN-0.2, respectively. On the other hand, the NF grain sizes increase only moderately with rising sintering temperature from 0.4 to 2 μm for $T_s = 1000 \text{ °C}$ to 1.1–5 μm for 1200 °C, whereas the grain size is barely affected by the sintering additive. The grain sizes of all magnetoelectric ceramics are listed in Tab. S1 (supporting information).

3.2. Magnetic behavior

The field-dependent magnetization curves measured at 300 K of NF-SBN+LN-0.2 ceramics sintered between 1000 and 1200 °C are exemplarily shown in Fig. 4. The analogous magnetization curves of the other ceramic samples are shown in Fig. S4 (supporting information). Data have been normalized with respect to the nominal NiFe_2O_4 fraction. Because of the ferrimagnetic nature of NiFe_2O_4 the ceramics reveal hysteresses with very low coercivity values between about 5 and 33 Oe. The saturation magnetizations (M_s) for the composite samples were calculated by extrapolating the magnetization at high field to $H = 0$ due to the presence of small amounts of paramagnetic secondary phases as aforementioned [25, 38–40]. The saturation magnetizations at 300 K of the composite ceramics are between $44.8(2)$ and $47.8(2) \text{ emu g}^{-1}$ and thus slightly lower than to the value of $49.7(1) \text{ emu g}^{-1}$ ($2.09(1) \mu_B \text{ f. u.}^{-1}$) for pure NiFe_2O_4 sintered under the same conditions. Additionally, the M_s values of the composites decrease slightly with rising sintering temperature, e.g. from $47.8(2)$ to $44.9(2) \text{ emu g}^{-1}$ ($2.01(1) - 1.88(1) \mu_B \text{ f. u.}^{-1}$) after sintering from 1000° to 1200°C for NF-SBN+LN-0.2 samples (inset II in Fig. 4 and Fig. S4, supporting information). The lower M_s values, compared to bulk NiFe_2O_4 , and their decreasing trend with sintering temperature is most likely caused by the formation of non-ferro-/nonferrimagnetic $(\text{FeNi})\text{Nb}_2\text{O}_4$ secondary phases resulting in the formation of Ni/Fe- vacancies and possible oxygen vacancies. Such vacancies caused a weakening of the superexchange interactions and also lead to a change of the cation distribution between the tetrahedral and octahedral site in the ferrite phase [41–43].

3.3. Impedance spectroscopy

The development of the real part of the relative permittivity (ϵ_r') and dissipation factor ($\tan \delta$) with the applied frequency at room temperature for ceramics sintered at 1100 °C is exemplarily shown in Fig. 5. All composite ceramics reveal slightly decreasing permittivities and $\tan \delta$ values with rising frequency (see also Fig. S5, supporting information), most likely caused by the Maxwell–Wagner interface polarisation of the electrically conductive NiFe_2O_4 grains surrounded by the insulating $\text{Sr}_{0.5}\text{Ba}_{0.5}\text{Nb}_2\text{O}_6$ matrix [44,45].

The temperature dependence of ϵ_r' and $\tan \delta$ at a frequency of 1 kHz is demonstrated for samples sintered at 1100 °C in Fig. 6. The permittivity values of all samples (see also Fig. S6, supporting information) rise with temperature up to 200 °C, whereas a permittivity maximum, which reflects the diffuse phase transition (Curie-range [34,46]) of $\text{Sr}_{0.5}\text{Ba}_{0.5}\text{Nb}_2\text{O}_6$ was not observed. Increasing permittivity values at higher temperatures are connected with an increase in the loss tangents, most likely due to a decreasing resistivity of these samples.

The conductivities of the magnetoelectric ceramics are low ($\sigma_{\text{DC}} \ll 10^{-7} \text{ S cm}^{-1}$) at room temperature, hence the high-temperature impedance data were fitted by an equivalent circuit consisting of one or two resistance-capacitor (RC) elements including a constant phase-shift element. The specific complex impedance (ρ^*) for a single RC element is described by [47]:

$$\rho^* = \frac{\rho_{\text{DC}}}{1 + (i\omega\tau)^\beta} \quad (1)$$

where, β is the constant phase-shift (CPE) coefficient and $\tau = \rho_{\text{DC}}\epsilon\epsilon_0$. The

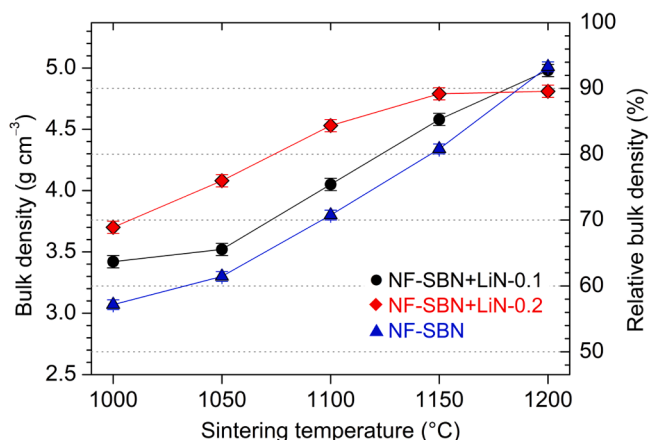


Fig. 2. Bulk densities of composite ceramic bodies after sintering at various temperatures for 1 h (heating-/cooling rate 5 K min^{-1}).

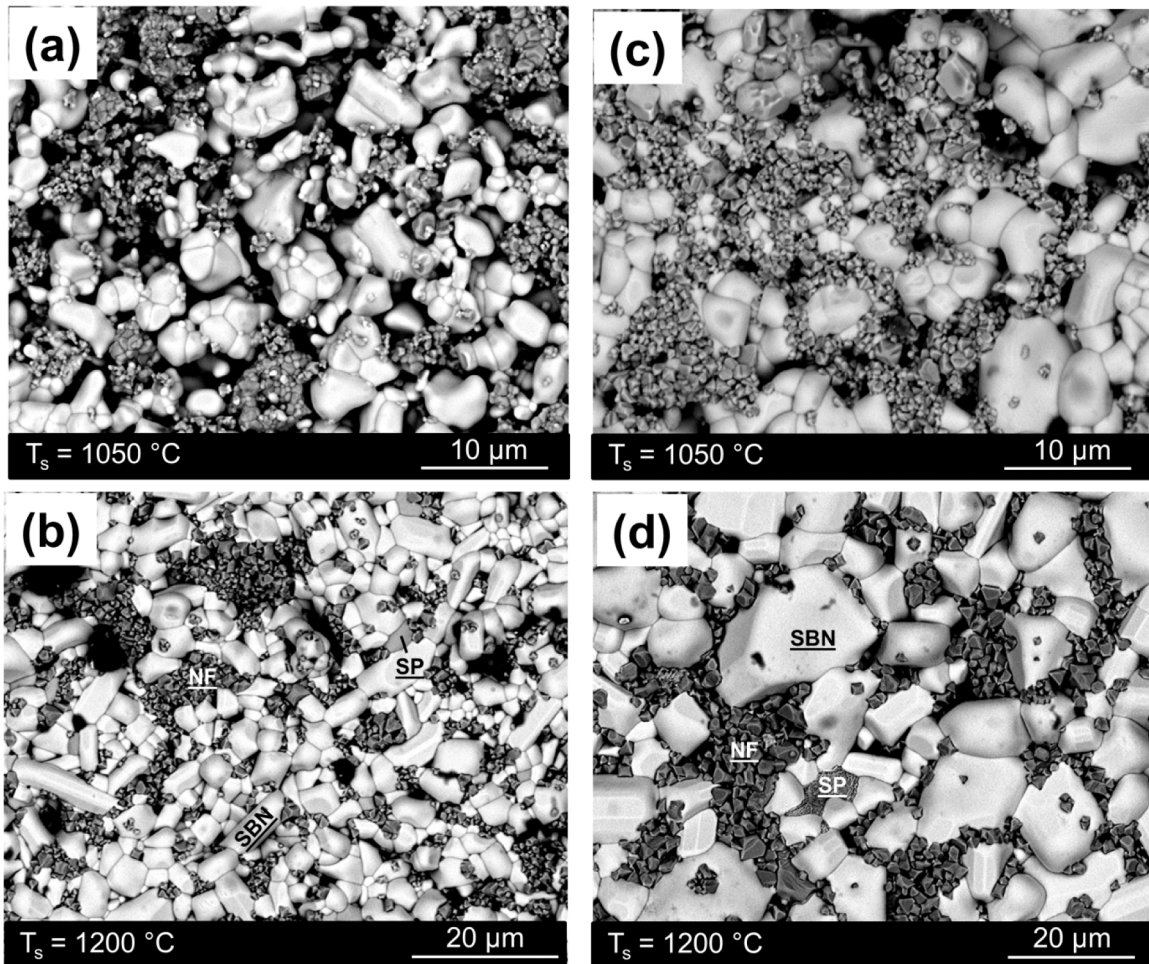


Fig. 3. SEM-BSE surface images of selected NF-SBN (a,b) and NF-SBN+LN-0.2 (c,d) ceramic bodies sintered at the indicated temperatures (T_s) for 1 h. The assignment of the grains is shown in (b) and (d) (NF = NiFe_2O_4 , SBN = $\text{Sr}_{0.5}\text{Ba}_{0.5}\text{Nb}_2\text{O}_4$, SP = secondary phase).

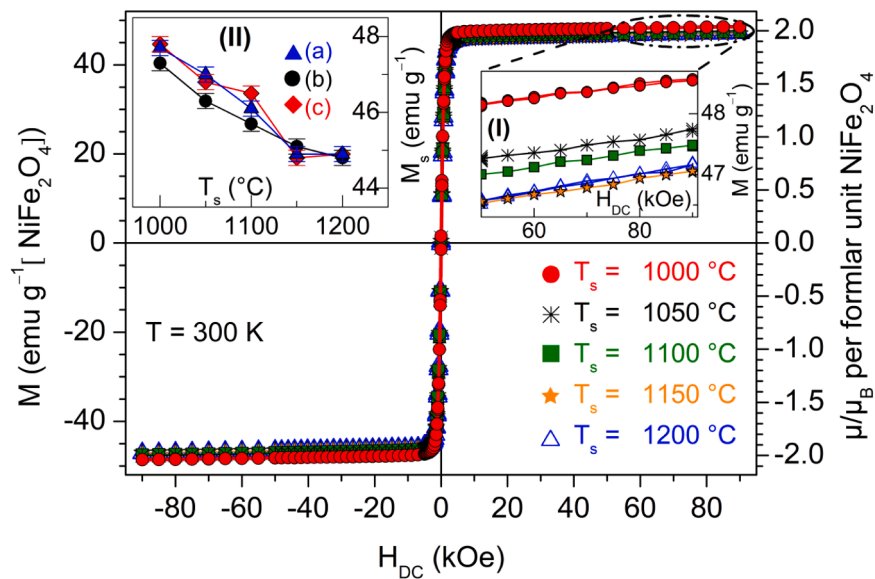


Fig. 4. Field dependence of the magnetization at 300 K for NF-SBN+LN-0.2 composite ceramics sintered at the indicated temperatures (T_s) for 1 h. Inset I shows a magnification at high magnetic fields. Inset II shows the saturation magnetization (M_s) depending on the sintering temperatures for (a) NF-SBN, (b) NF-SBN+LN-0.1, and (c) NF-SBN+LN-0.2 ceramics. The magnetization values are given with respect to the nominal NiFe_2O_4 content.

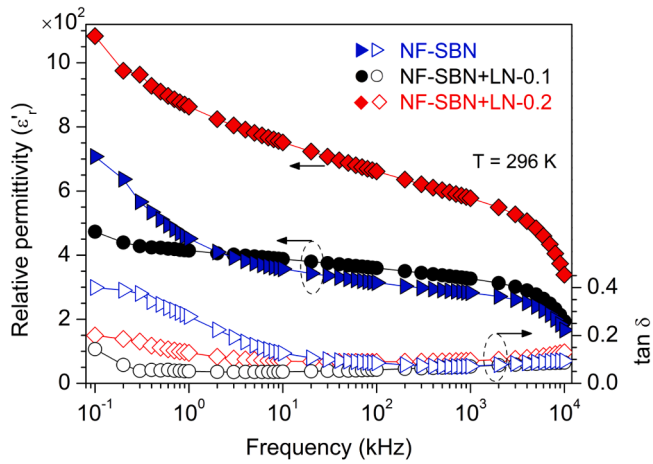


Fig. 5. Frequency dependence of ϵ_r' (closed symbols) and $\tan \delta$ (open symbols) at 296 K for the indicated magnetoelectric ceramic bodies sintered at 1100 °C for 1 h.

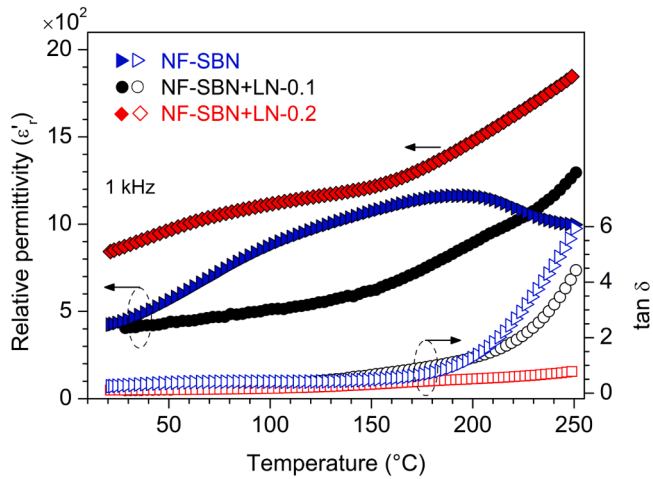


Fig. 6. Temperature dependence of ϵ_r' (closed symbols) and $\tan \delta$ (open symbols) at 1 kHz for the indicated magnetoelectric ceramic bodies sintered at 1100 °C for 1 h. For the sake of clarity every third data point is represented by a symbol.

Cole-Cole plots of composite ceramics sintered up to 1100 °C show one single semicircular arcs (Fig. S7, supporting information). The resultant calculated permittivities are between $6.9 \cdot 10^2 - 4.5 \cdot 10^3$ indicating that this single relaxation process can be assigned to the bulk effect only. On the other hand, the Cole-Cole plots (Fig. S8, supporting information) of the composites sintered at 1150 and 1200 °C can be well described by two RC elements connected in series suggesting two different electrical transport processes. The calculated permittivities for these two processes are between $3.7 \cdot 10^3 - 7.9 \cdot 10^3$ and $1.6 \cdot 10^4 - 4.1 \cdot 10^4$, respectively. According to Irvine et al. [48] the higher permittivity values can be assigned to grain boundary contributions, whereas the lower values represents the bulk contribution. From the fit of the data, also the DC resistivities were obtained. As seen in Fig. 7, the specific DC resistivities (ρ_{DC}) slightly increase for $T_s = 1050$ °C and then decrease with rising sintering temperature. Ceramics with the addition of LiNbO₃ NF-SBN+LN- x ($x = 0.1, 0.2$) show significantly higher resistivity values (about one order of magnitude) than the NF-SBN composites ceramics.

3.4. Magnetoelectric properties

Fig. 8 shows the dependence of the magnetoelectric coefficient (α_{ME})

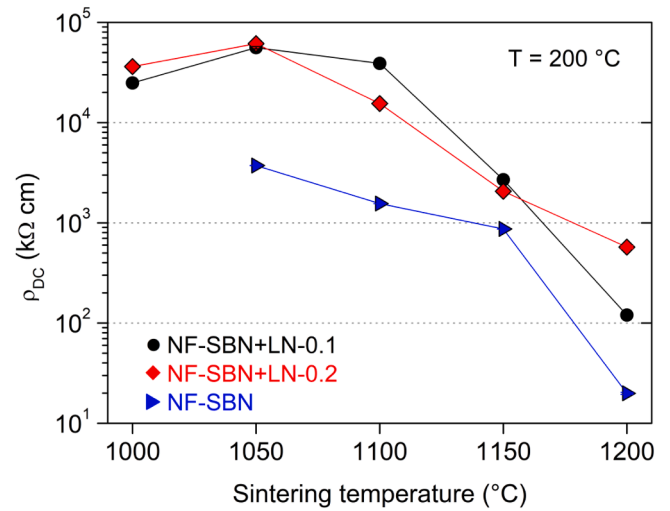


Fig. 7. Evolution of the specific DC resistivity with sintering temperature for the indicated magnetoelectric composite ceramics. The uncertainties of the data are smaller than the symbol sizes (less than 4 %).

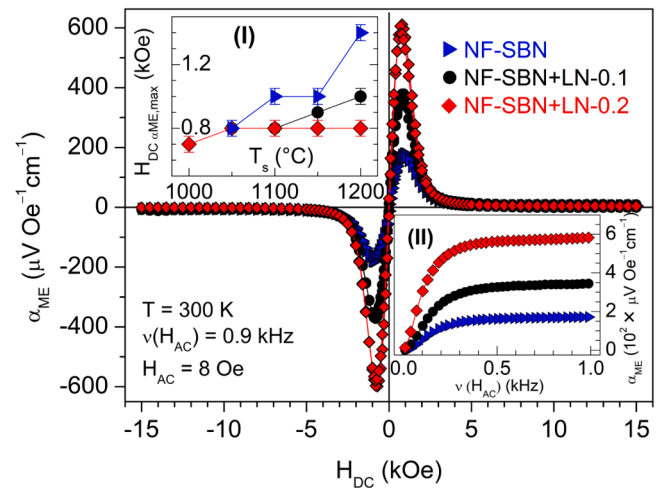


Fig. 8. Magnetoelectric coefficient (α_{ME}) vs. magnetic DC field for composite ceramics sintered at 1100 °C for 1 h. Inset I shows the evolution of $H_{DC\alpha_{ME,max}}$ with sintering temperature. Inset II shows the frequency dependence (H_{AC}) of α_{ME} at $H_{DC\alpha_{ME,max}}$ for composites sintered at 1100 °C. For the sake of clarity, in inset II every 10th data point is represented by a symbol.

measured at 300 K on the static magnetic field (H_{DC}) for composite ceramics fired at 1100 °C. Composites sintered at other temperatures exhibit analogous behaviors as demonstrated in Fig. S9 (supporting information). Starting from 15 kOe, α_{ME} remains very small until approximately 5 kOe and then increases to a maximum ($\alpha_{ME,max}$) at $H_{DC} \approx 1$ kOe and nearly vanishes at zero field, i. e. only very small remanences were observed and the coercive fields are smaller than 40 Oe. For negative fields an inverse behavior occurs. As can be seen in Fig. 9, $\alpha_{ME,max}$ strongly depends on the sintering temperature. Considering the impedance results, we assume that the decrease of $\alpha_{ME,max}$ for the higher sintering temperatures is due to an increase of conductivity resulting in an inner discharging. As seen in Fig. 9, the maximum of the magnetoelectric coefficient increases with the addition of LiNbO₃. We found maximum α_{ME} values of 180(10) $\mu\text{V Oe}^{-1} \text{cm}^{-1}$ and 379(20) $\mu\text{V Oe}^{-1} \text{cm}^{-1}$ after sintering at 1100 °C for NF-SBN and NF-SBN+LN-0.1 ceramics, while NF-SBN+LN-0.2 even shows a value of 803(43) $\mu\text{V Oe}^{-1} \text{cm}^{-1}$ after sintering at 1050 °C ($\nu(H_{AC}) = 900$ Hz). This increase of α_{ME} by the addition of the additive LiNbO₃ most likely is the result of higher

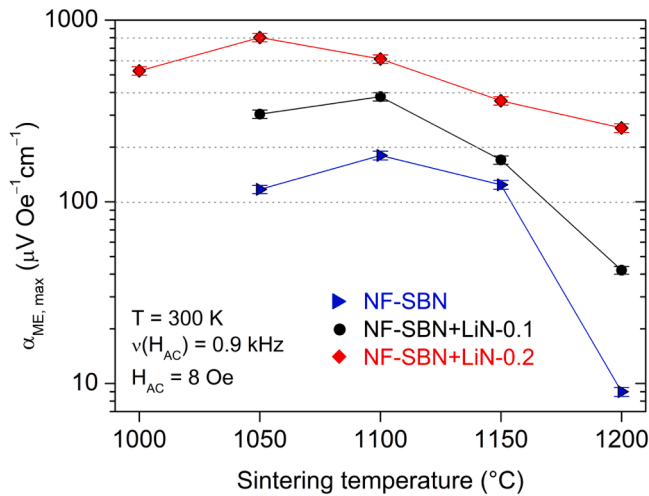


Fig. 9. Maximum magnetolectric coefficient ($\alpha_{ME,max}$) depending on the sintering temperature for the investigated composite ceramics.

bulk densities and significant higher grain sizes of the ferroelectric SBN phase. Additionally, the NF-SBN+LN- x samples possess significantly higher resistivity values (Fig. 7), even after sintering at high temperatures, which reduce an inner discharging of the samples. The outcome of the higher densification and lower resistivity is an improved coupling between the ferrimagnetic and ferroelectric grains. As pointed out in our previous paper [34] reaction between $Sr_{0.5}Ba_{0.5}Nb_2O_6$ and $LiNbO_3$ leads to a solid solution which can be described by the formula $Li_y(Sr_{0.5}Ba_{0.5})_{1-y/2}Nb_2O_6$ [49]. Therefore, a possible increase of the piezoelectric coefficient due to the partial substitution of Ba^{2+}/Sr^{2+} by Li^+ cannot be excluded as an additional reason for increasing α_{ME} , [50,51]. Depending on the sintering temperature, the H_{DC} field at which α_{ME} reaches its maximum ($H_{DC,max}$) slightly varies between 0.7 and 1.4 kOe as plotted in inset I of Fig. 8. For NF-SBN ceramics, we observed a considerable systematic increase of $H_{DC,max}$ with sintering temperature, while for NF-SBN+LN-0.2 ceramics $H_{DC,max}$ remains nearly constant and for NF-SBN+LN-0.1 a slight increase was found for $T_s > 1100$ °C. The inset II in Fig. 8 demonstrates the evolution of α_{ME} at $H_{DC,max}$ at 300 K depending on the frequency of the AC driving field for samples sintered at 1100 °C. All magnetolectric composites reveal an increase of α_{ME} up to 300–400 Hz, whereas α_{ME} is nearly constant at higher frequencies. Investigations by Bichurin and Petrov [52] showed that charge accumulation in 0–3 composites results in an inverse Maxwell-Wagner-type relaxation leading to an increasing charging of the capacitance with frequency, which saturates at higher frequencies. A similar behavior was also observed in e.g. $CoFe_2O_4$ – $Ba_{0.5}Sr_{0.5}Nb_2O_6$

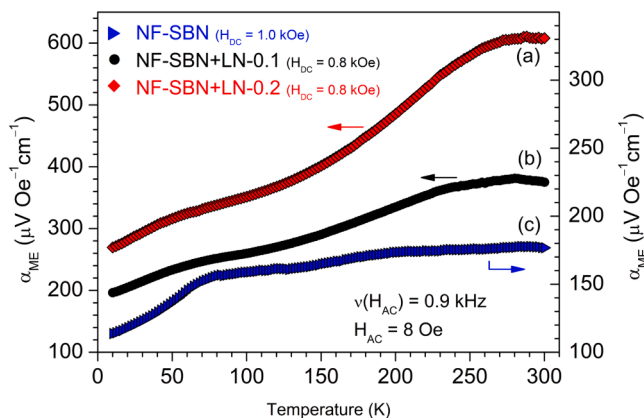


Fig. 10. α_{ME} versus temperature measured at the field at which the maximum α_{ME} appeared ($H_{DC,\alpha_{ME,max}}$) for composites sintered at 1100 °C for 1 h.

and $CoFe_2O_4$ – $BaTiO_3$ composites, respectively [15,28].

As seen in Fig. 10, temperature depended measurements of the magnetolectric coefficient during cooling show a decreasing α_{ME} at lower temperatures due to the decreasing piezoelectric/ferroelectric character of strontium barium niobate at low temperature [20, 53–55]. Measurements of α_{ME} versus H_{DC} at different temperatures between 50 and 300 K show that the magnetic DC field ($H_{DC,max}$) at which α_{ME} reaches its maximum does not shift with the measurement temperature (Fig. S10, supporting information). Therefore, the trend of decreasing α_{ME} at lower temperatures is due to a reduced magnetolectric coupling and not due to a shift of $H_{DC,max}$. This behavior supports the strain-mediated origin of α_{ME} [56].

The magnetolectric effect in composite materials is generally explained by a mechanic coupling between the magnetostrictive and the piezoelectric component. Therefore, the evolution of α_{ME} depending on H_{DC} is influenced by the magnetostriction and, consequently, the integration of α_{ME} over H_{DC} should reflect the course of the magnetostrictive coefficient (λ), qualitatively ($\lambda \sim \int \alpha_{ME} dH$) [57,58]. Fig. 11 and Fig. S11 (supporting information) show the integral of α_{ME} depending on H_{DC} in comparison with the static magnetostrictive coefficient data of $NiFe_2O_4$ taken from Anantharamaiah et al. [59] and Karpova et al. [60]. The evolution of the magnetostriction by Karpova et al. [60] was only measured for positive magnetic fields. It can be seen that a positive α_{ME} corresponds to a negative slope of λ . The integral of α_{ME} saturates at a field of > 3 kOe while the magnetostriction saturates already at about 1.5–2 kOe. This broadening of the $\int \alpha_{ME} dH$ curve compared to λ is probably due to the surrounding ferroelectric component which induces strain (pressure) into the $NiFe_2O_4$ grains. A similar behaviour was reported for Ni – $BaTiO_3$ composites [61]. In general, the magnetostriction mainly is influenced by particle size, pressure, and annealing temperature [62–64].

4. Conclusion

Magnetolectric $(NiFe_2O_4)_{0.3}$ – $(Sr_{0.5}Ba_{0.5}Nb_2O_6)_{0.7}$ composites with the addition of $LiNbO_3$ as sintering aid were synthesized by the conventional mixed-oxide method. Due to the sintering aid the densities of the ceramic increase significantly and the addition of $LiNbO_3$ leads to a significant growth of the $Sr_{0.5}Ba_{0.5}Nb_2O_6$ grains, while the size of the $NiFe_2O_4$ grains remains nearly unaffected. The microstructure of the ceramic bodies reveals a 0–3 connectivity. Temperature-dependent measurements show increasing permittivities and $\tan \delta$ values. The DC resistivity decreases with higher sintering temperature of the composite ceramics, whereas it increases with the addition of $LiNbO_3$. The field dependence of the magnetolectric coefficient (α_{ME}) shows maxima/

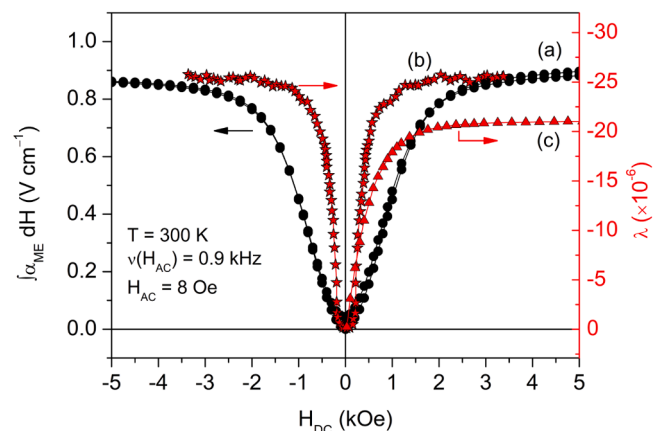


Fig. 11. Integral of α_{ME} of NF-SBN+LN-0.2 (a) sintered at 1100 °C compared to the static magnetostriction (λ) of $NiFe_2O_4$ (after Anantharamaiah et al. [45] (b) and Karpova et al. [46] (c)).

minima at H_{DC} between ± 0.7 and ± 1.4 kOe depending on sintering temperature. The maximum magnetoelectric coefficient considerably increases by addition of LiNbO_3 from 180(10) to 803(43) $\mu\text{V Oe}^{-1} \text{cm}^{-1}$ (@ 900 Hz). Temperature-dependent measurements show that α_{ME} becomes smaller at lower temperatures. Here, we examined for the first time the effect of sintering aids on the magnetoelectric behaviour. The investigations show that LiNbO_3 does not only influence densification and grain growth of composite ceramics, but also it is able to improve the magnetoelectric output. These results may be applicable for other magnetoelectric composites and therefore potentially offer a way for improved magnetoelectric properties.

Declaration of Competing Interest

The authors declare that they have no known competing financial interests or personal relationships that could have appeared to influence the work reported in this paper.

Appendix A. Supporting information

Supplementary data associated with this article can be found in the online version at [doi:10.1016/j.jeurceramsoc.2023.06.040](https://doi.org/10.1016/j.jeurceramsoc.2023.06.040).

References

- [1] D.N. Astrov, The magnetoelectric effect in antiferromagnetics, *Sov. Phys. JETP* 11 (1960) 708–709.
- [2] J.M. Caicedo, J.A. Zapata, M.E. Gómez, P. Prieto, Magnetoelectric coefficient in BiFeO_3 compounds, *J. Appl. Phys.* 103 (2008) 07E306.
- [3] G.T. Rado, V.J. Folen, Observation of the magnetically induced magnetoelectric effect and evidence for antiferromagnetic domains, *Phys. Rev. Lett.* 7 (1961) 310–311.
- [4] R.E. Newnham, D.P. Skinner, L.E. Cross, Connectivity and piezoelectric-pyroelectric composites, *Mat. Res. Bull.* 13 (1978) 525–536.
- [5] W.P. Wang, H. Yang, T. Xian, R.C. Yuc, Observation of abnormal magnetoelectric behavior in 0-3 type CoFe_2O_4 - BaTiO_3 nanocomposites, *Chem. Phys. Lett.* 618 (2015) 72–77.
- [6] S. Chileo, C. Pascual-Gonzalez, M. Alguero, I.M. Reaney, P. Postolache, L. Mitoseriu, K. Reichmann, A. Feteira, Yttrium iron garnet/barium titanate multiferroic composites, *J. Am. Ceram. Soc.* 99 (2016) 1609–1614.
- [7] S.Q. Ren, L.Q. Weng, S.-H. Song, F. Li, J.G. Wan, M. Zeng, $\text{BaTiO}_3/\text{CoFe}_2\text{O}_4$ particulate composites with large high frequency magnetoelectric response, *J. Mater. Sci.* 40 (2005) 4375–4378.
- [8] A. Hanumaiah, T. Bhimasankaram, S.V. Suryanarayana, G.S. Kumar, Dielectric behaviour and magnetoelectric effect in cobalt ferrite-barium titanate composites, *Bull. Mater. Sci.* 17 (1994) 405–409.
- [9] K. Li, D.-L. Shi, Y. Zhu, Y. Wang, H. Lai-wa Chan, S. Peng, Enhanced magnetoelectric coupling in cobalt ferrite/lead lanthanum zirconate titanate 0-3 composites through phase boundary modification, *Mater. Chem. Phys.* 143 (2013) 34–40.
- [10] R.A. Islam, J. Jiang, F. Bai, D. Viehland, S. Priya, Correlation between structural deformation and magnetoelectric response in $(1-x)\text{Pb}(\text{Zr}_{0.52}\text{Ti}_{0.48})\text{O}_3$ - $x\text{NiFe}_{1.9}\text{Mn}_{0.1}\text{O}_4$ particulate composites, *Appl. Phys. Lett.* 91 (2007), 162905.
- [11] S. Mokhtari, H. Ahmadvand, M.J. Fesharaki, H. Papi, P. Kameli, H. Salamati, Complex magnetoelectric effect in multiferroic composites: the case of PFN-PT/ $(\text{Co,Ni})\text{Fe}_2\text{O}_4$, *J. Phys. D: Appl. Phys.* 52 (2019), 505001.
- [12] J. van den Boomgaard, R.A.J. Born, A sintered magnetoelectric composite material BaTiO_3 - $\text{Ni}(\text{Co,Mn})\text{Fe}_2\text{O}_4$, *J. Mater. Sci.* 13 (1978) 1538–1548.
- [13] R. Gao, Z. Wang, G. Chen, X. Deng, W. Cai, C. Fu, Influence of core size on the multiferric properties of CoFe_2O_4 @ BaTiO_3 core shell structured composites, *Ceram. Int.* 44 (2018) S84–S87.
- [14] T. Ramesh, V. Rajendar, S.R. Murthy, CoFe_2O_4 - BaTiO_3 multiferroic composites: role of ferrite and ferroelectric phases on the structural, magneto dielectric properties, *J. Mater. Sci.: Mater. Electron* 28 (2017) 11779–11788.
- [15] T. Walther, U. Straube, R. Köferstein, S.G. Ebbinghaus, Hysteretic magnetoelectric behavior of CoFe_2O_4 - BaTiO_3 composites prepared by reductive sintering and reoxidation, *J. Mater. Chem. C* 4 (2016) 4792–4799.
- [16] A. Chaudhuri, K. Mandal, Large magnetoelectric properties in CoFe_2O_4 @ BaTiO_3 core-shell nanocomposites, *J. Magn. Magn. Mater.* 377 (2015) 441–445.
- [17] S. Tiwari, S. Vitta, Magnetoelectric and magnetodielectric coupling and microwave resonator characteristics of $\text{Ba}_{0.5}\text{Sr}_{0.5}\text{Nb}_2\text{O}_6/\text{CoCr}_{0.4}\text{Fe}_{1.6}\text{O}_4$ multiferroic composite, *Sci. Rep.* 8 (2018) 11619.
- [18] Y.H. Tang, X.M. Chen, Y.J. Li, X.H. Zheng, Dielectric and magnetoelectric characterization of $\text{CoFe}_2\text{O}_4/\text{Ba}_{0.55}\text{Sr}_{0.25}\text{Ca}_{0.2}\text{Nb}_2\text{O}_6$ composites, *Mater. Sci. Eng. B* 116 (2005) 150–155.
- [19] S.S. Rathore, S. Vitta, Large low field room temperature magneto-dielectric response from $(\text{Sr}_{0.5}\text{Ba}_{0.5})\text{Nb}_2\text{O}_6/\text{Co}(\text{Cr}_{0.4}\text{Fe}_{1.6})\text{O}_4$ Bulk 3-0 composites, *Mater. Sci. Eng. B* 204 (2016) 1–7.
- [20] A.A. Ballmann, H. Brown, The growth and properties of strontium barium metaniobate $\text{Sr}_x\text{Ba}_{1-x}\text{Nb}_2\text{O}_6$, a tungsten bronze ferroelectric, *J. Cryst. Growth* 1 (1967) 311–314.
- [21] R. Köferstein, F. Oehler, S.G. Ebbinghaus, Investigations of nano-crystalline $\text{Sr}_{0.5}\text{Ba}_{0.5}\text{Nb}_2\text{O}_6$ and bulk ceramics synthesized by a polymerization method using PEG400, *J. Eur. Ceram. Soc.* 39 (2019) 1156–1163.
- [22] S.S. Rathore, S. Vitta, Enhanced dielectric constant and relaxor behavior realized by dual stage sintering of $\text{Sr}_{0.5}\text{Ba}_{0.5}\text{Nb}_2\text{O}_6$, *AIP Conf. Proc.* 1591 (2014) 133–135.
- [23] S. Lee, C.A. Randall, Z.-K. Liu, Modified phase diagram for the barium oxide-titanium dioxide system for the ferroelectric barium titanate, *J. Am. Ceram. Soc.* 90 (2007) 2589–2594.
- [24] T. Müller, H.-P. Abicht, Influence of the cubic/hexagonal phase transition on the mechanical strength of barium titanate ceramics, *cfi/Ber, DKG* 77 (2000) E26–E31.
- [25] R. Köferstein, T. Walther, D. Hesse, S.G. Ebbinghaus, Fine-grained BaTiO_3 - MgFe_2O_4 composites prepared by a pechini-like process, *J. Alloy. Compd.* 638 (2015) 141–147.
- [26] K. Kamishima, Y. Nagashima, K. Kakizaki, N. Hiratsuka, K. Watanabe, T. Mise, H. Naganuma, S. Okamura, Simple process synthesis of BaTiO_3 - $(\text{Ni,Zn,Cu})\text{Fe}_2\text{O}_4$ ceramic composite, *J. Phys. Soc. Jpn.* 77 (2008), 064801.
- [27] R.R. Neurgaonkar, W.K. Cory, J.R. Oliver, E.J. Sharp, G.L. Wood, G.J. Salamo, Growth and optical properties of ferroelectric tungsten bronze crystals, *Ferroelectrics* 142 (1993) 167–188.
- [28] R. Köferstein, F. Oehler, S.G. Ebbinghaus, Fine-grained magnetoelectric $\text{Sr}_{0.5}\text{Ba}_{0.5}\text{Nb}_2\text{O}_6$ - CoFe_2O_4 composites synthesized by a straightforward one-pot method, *Mater. Chem. Phys.* 278 (2022), 125616.
- [29] S.R. Jigajeni, A.N. Tarale, D.J. Salunkhe, P.B. Joshi, S.B. Kulkarni, Dielectric, magnetoelectric and magnetodielectric properties in CMFO-SBN composites, *Ceram. Int.* 39 (2013) 2331–2341.
- [30] S.R. Jigajeni, M.M. Sutar, S.M. Salunkhe, P.B. Joshi, Investigation on magnetoelectric and dielectric properties of $\text{Co}_{0.9}\text{Mn}_{0.3}\text{Fe}_{1.8}\text{O}_4$ - $\text{Sr}_{0.5}\text{Ba}_{0.5}\text{Nb}_2\text{O}_6$ composites, *J. Mater. Sci.: Mater. Electron* 23 (2012) 1678–1687.
- [31] N. Kitahara, H. Kageyama, T. Kawasaki, K. Abe, H. Itoh, J. Takahashi, Low-temperature fabrication of NiCuZn ferrite- $(\text{Ba}_{0.7}\text{Sr}_{0.3})\text{TiO}_3$ composites using granulated powders, *J. Ceram. Soc. Jpn* 121 (2013) 54–61.
- [32] S.S. Veer, D.J. Salunkhe, S.V. Kulkarni, S.B. Kulkarni, P.B. Joshi, Effect of sintering aid on physical and magnetoelectric properties of $\text{La}_{0.7}\text{Sr}_{0.3}\text{MnO}_3$ - BaTiO_3 composites, *Indian J. Eng. Mater. Sci.* 15 (2008) 121–125.
- [33] D. liang Shi, K.H. Lam, K. Li, LPF-Doped core-shell structure based CFO/PLZT 0–3 magnetoelectric composite ceramics, *J. Alloy. Compd.* 617 (2014) 484–490.
- [34] R. Köferstein, S.G. Ebbinghaus, Effect of sintering additives on the densification and dielectric properties of $\text{Sr}_{0.5}\text{Ba}_{0.5}\text{Nb}_2\text{O}_6$ ceramics synthesized by a soft-chemistry method, *J. Solid State Chem.* 278 (2022), 123564.
- [35] M.A. Gabal, Y.M. Angari, Effect of chromium ion substitution on the electromagnetic properties of nickel ferrite, *Mater. Chem. Phys.* 118 (2009), 153160.
- [36] J. Ravez, A. Perron-Simon, P. Hagenmuller, Les phases de structure "bronzes de tungstène quadratiques": règles cristalochimiques, relations entre propriétés ferroélectriques et distorsions structurales, *Ann. Chim. I* (1976) 251–268.
- [37] R.R. Neurgaonkar, W.F. Hall, J.R. Oliver, W.W. Ho, W.K. Cory, Tungsten bronze $\text{Sr}_{1-x}\text{Ba}_x\text{Nb}_2\text{O}_6$: a case history of versatility, *Ferroelectrics* 87 (1988) 167–179.
- [38] I. Aegeer, A.H. Morrish, B.M. Wanklyn, Magnetization studies in transition-metal niobates: I. NiNb_2O_6 , *Phys. Rev. B* 15 (1977) 1465–1476.
- [39] C.B. Liu, R. Chen, X.Y. Yue, Y.J. Liu, M.M. Shi, H.P. Zhu, C. Domg, Y. Liu, Y.B. Han, J.F. Wang, Z.Z. He, Crystal growth, magnetic property and phase transition of the zigzag-chain antiferromagnet FeNbO_4 , *J. Magn. Magn. Mater.* 464 (2018) 108–111.
- [40] H. Ehrenberg, G. Wltschek, R. Theissmann, H. Weitzel, H. Fuess, F. Trouw, The magnetic structure of FeNbO_4 , *J. Magn. Magn. Mater.* 218 (2000) 261–265.
- [41] G. Hassnain Jaffari, A.K. Rumaiz, J.C. Woicik, S. Ismat Shah, Influence of oxygen vacancies on the electronic structure and magnetic properties of NiFe_2O_4 thin films, *J. Appl. Phys.* 111 (2012), 093906.
- [42] S. Singh, S. Munjal, N. Khare, Strain/defect induced enhanced coercivity in single domain CoFe_2O_4 nanoparticles, *J. Magn. Magn. Mater.* 386 (2015) 69–73.
- [43] J.-H. Cho, S. Cho, J.H. Lee, H. Palneedi, J.-H. Lee, H.-P. Kim, N.J. Lee, S. Tigunta, S. Pojprapai, S. Kim, J. Ryu, Y.S. Oh, S. Hong, W. Jo, Room-temperature multiferricity in NiFe_2O_4 and its magnetoelectric coupling intensified through defect engineering, *J. Am. Ceram. Soc.* 104 (2021) 6384–6392.
- [44] K.W. Wagner, Erklärung der dielektrischen Nachwirkungsvorgänge auf Grund Maxwellscher Vorstellungen, *Arch. Elektro* 2 (1914) 371–387.
- [45] A. Sakanas, R. Grigalaitis, J. Banys, L. Mitoseriu, V. Buscaglia, P. Nanni, Broadband dielectric spectroscopy of BaTiO_3 - $\text{Ni}_{0.5}\text{Zn}_{0.5}\text{Fe}_2\text{O}_4$ composite ceramics, *J. Alloy. Compd.* 602 (2014) 241–247.
- [46] K. Uchino, Relaxor Ferroelectric-based Ceramics, in: K. Uchino (Ed.), *Advanced Piezoelectric Materials Science and Technology*, Woodhead Publishing Limited, Cambridge, 2010, p. 111 (et seq).
- [47] F. Oehler, H.-T. Langhammer, S.G. Ebbinghaus, Preparation and dielectric properties of CaTaO_2N and SrNbO_2N ceramics, *J. Eur. Ceram. Soc.* 37 (2017) 2129–2136.
- [48] J.T.S. Irvine, D.C. Sinclair, A.R. West, Electroceramics: characterization by impedance spectroscopy, *Adv. Mater.* 2 (1990) 132–138.
- [49] In the formula $\text{Li}_y(\text{Sr}_{0.5}\text{Ba}_{0.5})_{1-y/2}\text{Nb}_2\text{O}_6$ (solid solution between $\text{Sr}_{0.5}\text{Ba}_{0.5}\text{Nb}_2\text{O}_6$ and LiNbO_3), y represents the molar fraction of LiNbO_3 which can be calculated from the x parameter as $y = x/(1+x/2)$.
- [50] R.R. Neurgaonkar, J.R. Oliver, W.K. Cory, L.E. Cross, D. Viehland, Piezoelectricity in tungsten bronze crystals, *Ferroelectrics* 160 (1994) 265–276.

- [51] W. Jiang, W. Cao, X. Yi, H. Chen, The elastic and piezoelectric properties of tungsten bronze ferroelectric crystals ($\text{Sr}_{0.7}\text{Ba}_{0.3}\text{NaNb}_5\text{O}_{15}$ and $(\text{Sr}_{0.3}\text{Ba}_{0.7})_2\text{NaNb}_5\text{O}_{15}$), *J. Appl. Phys.* 97 (2005), 094106.
- [52] M. Bichurin, V. Petrov, *Modeling of Magnetoelectric Effects in Composites*, Springer, Dordrecht, 2014, p. 45.
- [53] T. Volk, D. Isakov, V. Salobutin, L. Ivleva, P. Lykov, V. Ramzaev, M. Wöhlecke, Effects of Ni doping on properties of strontium–barium–niobate crystals, *Solid State Comm.* 130 (2004) 223–226.
- [54] B.-M. Jin, R. Guo, A.S. Bhalla, Piezoelectric properties and equivalent circuits of ferroelectric relaxor single crystals, *J. Mater. Sci.* 32 (1997) 2005–2058.
- [55] T.R. Volk, V.Yu Salobutin, L.I. Ivleva, N.M. Polozkov, R. Pankrath, M. Woehlecke, Ferroelectric properties of strontium barium niobate crystals doped with rare-earth metals, *Phys. Solid State* 42 (2000) 2129–2136.
- [56] J. van Suchtelen, Product properties: a new application of composite materials, *Philips Res. Rep.* 27 (1972) 28–37.
- [57] Y. Zhou, D. Maurya, Y. Yan, G. Srinivasan, E. Quandt, S. Priya, Self-biased magnetoelectric composites: an overview and future perspectives, *Energy Harvest. Syst.* 3 (2016) 1–42.
- [58] D.A. Filippov, V.M. Laletin, N.N. Poddubnaya, V.V. Shvartman, D.C. Lupascu, J. Zhang, G. Srinivasan, Magnetostriction via magnetoelectricity: using magnetoelectric response to determine the magnetostriction characteristics of composite multiferroics, *Tech. Phys. Lett.* 45 (2019) 1152–1154.
- [59] P.N. Anantharamaiah, B. Prerna Rao, H.M. Shashanka, J.A. Chelvane, V. Khopkar, B. Sahoo, Role of Mg^{2+} and In^{3+} substitution on magnetic, magnetostrictive and dielectric properties of NiFe_2O_4 ceramics derived from nanopowders, *Phys. Chem. Chem. Phys.* 23 (2021) 1694–1705.
- [60] T. Karpova, V. Vassiliev, E. Vladimirova, V. Osotov, M. Ronkin, A. Nosov, Synthesis of ultradisperse NiFe_2O_4 spinel by thermal decomposition of citrate precursors and its magnetic properties, *Ceram. Int.* 38 (2012) 373–379.
- [61] T. Buttler, T. Walther, K. Dörr, S.G. Ebbinghaus, Preparation and magnetoelectric behavior of Ni/BaTiO_3 heterostructures with 0-3 connectivity, *Phys. Stat. Solidi B* 257 (2020) 1900622.
- [62] S.D. Bahme, P.A. Joy, Enhanced magnetostrictive properties of CoFe_2O_4 synthesized by an autocombustion method, *Sens. Actuators A* 137 (2007) 256–261.
- [63] K. Khaja Mohaideen, P.A. Joy, Influence of initial particle size on the magnetostriction of sintered cobalt ferrite derived from nanocrystalline, *Powders, J. Magn. Mater.* 346 (2013) 96–102.
- [64] K. Venkata Siva, S. Sudersan, A. Arocklarajan, Bipolar magnetostriction in CoFe_2O_4 : effect of sintering, measurement temperature, and prestress, *J. Appl. Phys.* 128 (2020), 103904.